AIAA SciTech Forum
8-12 January 2024, Orlando, FL
AIAA SCITECH 2024 Forum

10.2514/6.2024-1286

Online Control and Moment of Inertia Estimation of Tethered Debris

Liam Field* and Derek Bourabah†
Mechanical and Aerospace Engineering, 211 Bell Hall, Buffalo, NY, 14260, United States

Eleonora M. Botta‡
Mechanical and Aerospace Engineering, 211 Bell Hall, Buffalo, NY, 14260, United States

Tethered capture of space debris is a promising method of active debris removal (ADR), but has numerous well-known challenges in the post-capture phase. Control of the system in this phase is complicated by nonlinear dynamics with the potential of chaotic motion, unknown debris parameters, and debris tumbling. The inherent uncertainty present in the system and the need for control often necessitate the estimation of debris states and parameters such that the post-capture system can remain controlled. To this end, a relative distance Proportional-Integral-Derivative (PID) control and an Unscented Kalman Filter (UKF) are implemented during the post-capture phase of an ADR mission. It is assumed that some debris (target) states and properties are unknown to the chaser, requiring the estimation of the attitude, angular rates, and principal moments of inertia of the target. For estimating these states, the UKF uses measurements of the tether tension magnitude and pixel coordinates of feature points on the target provided by a camera mounted on the chaser. Both estimation and control are done simultaneously, simulating online estimation and control of an ADR mission. The PID control was found to maintain safe conditions when using the estimated states in two separate Monte-Carlo simulations, differing in the measurement frequency of the pixel coordinates, while the estimation of the principal moments of inertia of the debris was satisfactory.

I. Introduction

Multiple orbits around Earth are becoming increasingly congested due to increased launches of satellite constellations. Space debris poses a growing threat to all active space missions and has already been involved in collisions [1, 2]. A major contributor to the problem is large space debris, since impacts with it would generate clouds of additional smaller debris that would further clutter the near-earth orbits [3]. Numerous methods of debris removal have been suggested, with interest in promising methods involving tether-based capture (e.g., tethered nets, harpoons, and robots) [4–11].

Tether-based methods of debris capture, while promising, pose numerous difficulties for post-capture control. These difficulties include but are not limited to: flexible tethers being unable to support compression, largely unknown target properties, and nonlinear dynamics with the possibility of chaotic motion [12–14]. Post-capture control of the system is especially important for collision prevention between the chaser and debris, since these are physically connected. A few possible contributors to post-capture collision include tether winding around the target and whiplash of the target debris in the case of very high tensions [12, 15]. Aslanov and Yudintsev studied tether winding and discovered that slackness of the tether is a major cause of this problem [12]. One solution is to maintain a relative distance between the chaser and target that results in a taut tether. Multiple authors have applied proportional-integral-derivative (PID) control to maintain a desired relative distance between the chaser and debris and to control the debris attitude [16–18]. Winding of the tether may also be caused by tumbling debris, which may be mitigated through the use of attitude control methodologies such as a yo-yo mechanism, tension PID control, wave-based control, etc. [18–22]. While many control methods have been proposed, it is often found that the controls either require or would be improved by principal moment of inertia knowledge of the debris. However, as the debris is uncooperative and unresponsive, this information is often unknown.

In tethered debris systems, often only the ratios of the principal moments of inertia are found due to a lack of information on the affecting moments on the debris [23, 24]. In the case of tethered robots and robotic arm capture of

*PhD Student, Mechanical and Aerospace Engineering, 211 Bell Hall, Buffalo, NY 14260, Student member.
†PhD Student, Mechanical and Aerospace Engineering, 211 Bell Hall, Buffalo, NY 14260, Student Member.
‡Assistant Professor, PhD Student, Mechanical and Aerospace Engineering, 211 Bell Hall, Buffalo, NY 14260, Senior Member

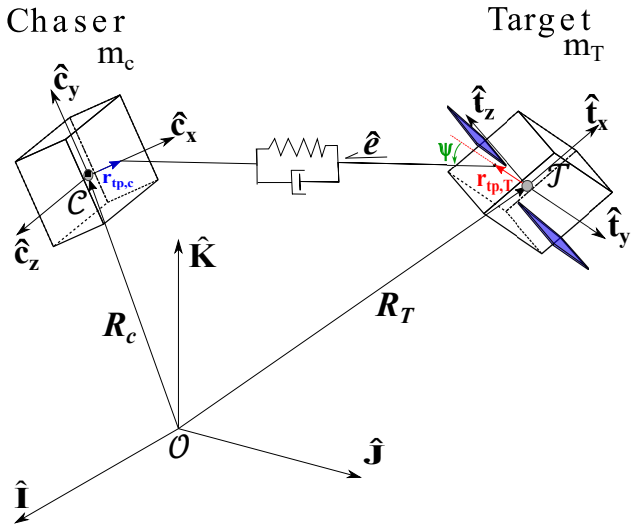

Fig. 1. System model with reference frames.

debris, the principal moments of inertia may more easily be estimated thanks to either the rigid connection between the chaser and target or because a known force may be applied to the target in the case of tethered robots [25–30]. In the case of passive capture of the debris, the principal moments of inertia are harder to estimate and work on this topic is scarce. Zhang et al. estimated one principal moment of inertia and the difference between the other two principal moments of inertia during retrieval of debris [31]. Prior work by the authors compared two Extended Kalman Filter (EKF) algorithms and an UKF for principal moment of inertia estimation using perfect knowledge of tension and angular rate measurements of the debris [32]. This work was then expanded to use tension measurements and a camera tracking two features on the debris using a UKF [33].

In prior work by the authors, estimation was performed offline, while the dynamics were integrated assuming the control had perfect knowledge of the system. In this work, instead, estimation and control are performed online, such that the controller no longer assumes perfect knowledge of the states of the system. The UKF is improved from prior work by means of the inclusion of an occlusion model that takes into account the debris orientation when generating pixel coordinate measurements of tracked features. The PID control is designed to obtain accurate estimation results of the principal moments of inertia while maintaining safe capture of the debris.

The remainder of this paper is organized as follows: First, the kinematics and dynamics of the tethered debris system along with the model of the camera are discussed in Section II. Then, the UKF, the controller design, and the online estimation and control algorithm are detailed in Section III. The simulation setup and results are presented in Section IV. Conclusions are provided in Section V.

II. System Models

The model of the tethered satellite system consists of two rigid bodies, the chaser craft (on which the camera and tension sensor are mounted) and the target, with an elastic tether pinned to both bodies. The target is modeled as a rectangular prism while the chaser is modeled as a cube. An image of the model can be found in Fig. 1, which includes important frame definitions and vectors. The inertial frame for the system is defined as $\mathcal{O} = [\hat{\boldsymbol{I}}, \hat{\boldsymbol{J}}, \hat{\boldsymbol{K}}]$, while the chaser and target body-fixed frames are $\mathcal{C} = [\hat{\boldsymbol{c}}_x, \hat{\boldsymbol{c}}_y, \hat{\boldsymbol{c}}_z]$ and $\mathcal{T} = [\hat{\boldsymbol{t}}_x, \hat{\boldsymbol{t}}_y, \hat{\boldsymbol{t}}_z]$, respectively. The angle ψ is the target alignment angle, indicating how far the tether is pointing away from the negative $\boldsymbol{t}_y$ face normal, and $\hat{\boldsymbol{e}}$ is the tether heading vector.

A. Rigid Body Model

The kinematics of the rigid bodies in the inertial reference frame are described by the inertial position $\boldsymbol{R}$ and velocity $\boldsymbol{V}$ of their centers of mass. It should be noted that the argument of time has been omitted for brevity. As the only external forces considered are the force of gravity and the chaser control thrust, the resulting translational kinematics

and dynamics for a given rigid body are

$$\dot{\boldsymbol{R}} = \boldsymbol{V} \tag{1a}$$

$$m\dot{\boldsymbol{V}} = -m\mu_e \frac{\boldsymbol{R}}{||\boldsymbol{R}||^3} + \boldsymbol{T} + \boldsymbol{U} \tag{1b}$$

where m is the respective satellite body mass, μ_e is the standard gravitational parameter of the Earth, $\boldsymbol{T}$ is the tether tension affecting the body and $\boldsymbol{U}$ is a vector of control forces. The control force is $\mathbf{0}$ for the target as it is uncooperative. The tether model is discussed in the following Section.

The attitude kinematics are described by an attitude quaternion expressed in the inertial reference frame as $\boldsymbol{q} = [\boldsymbol{q}_v, q_4]^T$, where $\boldsymbol{q}_v$ and q_4 are the vector and scalar components, respectively, and an angular velocity $\boldsymbol{\omega}$. The body angular velocity is expressed in its respective body-fixed frame as $\boldsymbol{\omega} = [\omega_x, \omega_y, \omega_z]^T$. The attitude kinematics and dynamics are then:

$$\dot{\boldsymbol{q}} = \frac{1}{2}\begin{bmatrix} I_{3x3}q_4 + S(\boldsymbol{q}_v) \\ -\boldsymbol{q}_v{}^T \end{bmatrix} \boldsymbol{\omega} \tag{2a}$$

$$\dot{\boldsymbol{\omega}} = J^{-1}\left(\boldsymbol{\tau} + \boldsymbol{r}_{tp,B} \times ({}^{\mathcal{B}}A^{O}\boldsymbol{T}) - \boldsymbol{\omega} \times J\boldsymbol{\omega}\right) \tag{2b}$$

where $S(\cdot)$ is the cross product matrix, J is the moment of inertia matrix of the body and $\boldsymbol{\tau}$ are any control torques. The tether attachment point with respect to a body-fixed frame is $\boldsymbol{r}_{tp,B}$, where B denotes either the chaser C or target T (see Fig. 1). With the assumption that the tether is rigidly connected to both bodies, $\boldsymbol{r}_{tp,B}$ is constant. The tension, which is expressed in the inertial frame, must be transformed by the rotation matrix ${}^{\mathcal{B}}A^{O}$. The notation is such that ${}^{\mathcal{B}}A^{O}$ transforms from the inertial frame O to the body-fixed frame $\mathcal{B}$. In congruence with the translational dynamics, the control torques are not present for the target. The kinematics and dynamics in Eq. (1a)-(2) can be cast into the first order form as follows:

$$\dot{\boldsymbol{X}} = \boldsymbol{f}\left(\boldsymbol{X}, \boldsymbol{U}, \boldsymbol{\tau}, t\right) \tag{3}$$

The system states $\boldsymbol{X}$ are composed of the chaser and target states such that

$$\boldsymbol{X} = \begin{bmatrix} \boldsymbol{X}^C \\ \boldsymbol{X}^T \end{bmatrix} \qquad \boldsymbol{X}^B = \begin{bmatrix} \boldsymbol{R}^B \\ \boldsymbol{V}^B \\ \boldsymbol{q}^B \\ \boldsymbol{\omega}^B \end{bmatrix} \tag{4}$$

where B denotes a given body.

B. Tether Model

The tether is modeled as a Kelvin-Voigt element that cannot support compression. The equation for tension, given stiffness k and damping c, is then

$$\boldsymbol{T} = \begin{cases} T\hat{\boldsymbol{e}} & \text{if} \quad (l > l_0) \wedge (T > 0), \\ 0 & \text{if} \quad (l \leq l_0) \vee (T \leq 0). \end{cases} \tag{5}$$

where $T = k(l - l_0) + c\dot{l}$, l_0 is the tether natural length, l is the current length and $\dot{l}$ is the length rate of change. It should be noted that the tension, as calculated here, is that applied to the target due to the direction of the tether heading vector $\hat{\boldsymbol{e}}$, depicted in Fig. 1. This vector is

$$\hat{\boldsymbol{e}} = \frac{\boldsymbol{R}_C +^{O} \boldsymbol{r}_{tp,C} - \boldsymbol{R}_T -^{O} \boldsymbol{r}_{tp,T}}{||\boldsymbol{R}_C +^{O} \boldsymbol{r}_{tp,C} - \boldsymbol{R}_T -^{O} \boldsymbol{r}_{tp,T}||} \tag{6}$$

where the tether attachment points $\boldsymbol{r}_{tp,C}$ and $\boldsymbol{r}_{tp,T}$ are expressed in the inertial frame. With this definition of the heading vector, l is the denominator of Eq. (6). The length rate is calculated by finding the relative velocity between the chaser and target attachment points, then projecting that vector onto $\hat{\boldsymbol{e}}$:

$$\dot{l} = (\boldsymbol{V}_C +^{O} \boldsymbol{A}^{C}\boldsymbol{\omega}_C \times^{C} \boldsymbol{r}_{tp,C} - \boldsymbol{V}_T -^{O} \boldsymbol{A}^{\mathcal{T}}\boldsymbol{\omega}_T \times^{\mathcal{T}} \boldsymbol{r}_{tp,T}) \cdot \hat{\boldsymbol{e}} \tag{7}$$

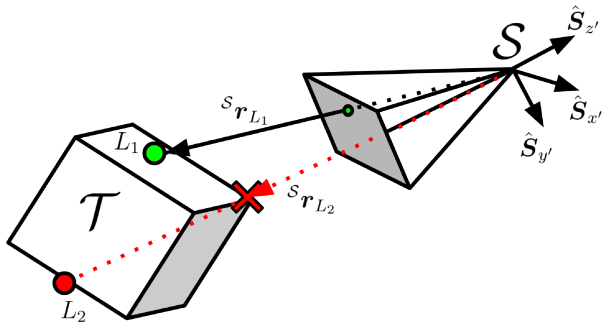

Fig. 2. Landmarks as seen in the camera frame

C. Camera Model

The camera on board the chaser is simulated using a pinhole camera projection model given by:

$$\begin{bmatrix} d_{x'} \\ d_{y'} \end{bmatrix} = \begin{bmatrix} c_{x'} + s_{x'}\left(c_{x'} - \frac{\epsilon_1}{\epsilon_3}\right) \\ c_{y'} - s_{y'}\left(c_{y'} - \frac{\epsilon_2}{\epsilon_3}\right) \end{bmatrix} \tag{8a}$$

$$\boldsymbol{\epsilon} = \begin{bmatrix} \epsilon_1 \\ \epsilon_2 \\ \epsilon_3 \end{bmatrix} = \begin{bmatrix} f & 0 & c_{x'} \\ 0 & f & c_{y'} \\ 0 & 0 & 1 \end{bmatrix} \cdot {}^{s}\boldsymbol{r}_L \tag{8b}$$

where the center of the image is provided by $c_{x'}$ and $c_{y'}$ in pixel coordinates, and the scale between the image space and world space is denoted by $s_{x'}$ and $s_{y'}$. These scales can be determined by dividing the image resolution by the sensor size. The focal length is given by f and a landmark position in the camera frame is denoted as ${}^{s}\boldsymbol{r}_L$. Although the pinhole camera model will transform any point in 3D space to the pixel coordinates, various landmarks can be blocked from view depending on the orientation of the debris. During such times, the obscured landmark is said to be occluded, which is further discussed in Section II.D.

D. Occlusion Model

Occlusion occurs when a landmark on the debris is obscured by an object between the landmark and the camera. In this work, occlusion will occur when the orientation of the debris causes a landmark to be obscured by another part of the debris due to its orientation in space. Fig. 2 demonstrates the camera frame where a landmark, L_1, is visible and another landmark, L_2, is occluded. As the target is assumed to be a rectangular prism, occlusion may be modeled by simply checking the normal vector of the face a landmark is located on, $\hat{\boldsymbol{n}}_L$. The landmark is considered to be visible if the normal vector is facing toward the camera, and is not visible when the normal vector is facing away from the camera. An equation to denote this condition is given as:

$${}^{S}\hat{\boldsymbol{n}}_L \cdot \hat{\boldsymbol{S}}_{z'} > 0 \tag{9}$$

where the condition is true when the landmark is visible and false when the landmark is occluded. When a landmark is occluded, no pixel coordinate measurement is provided to the UKF for that time step. If the landmark is visible to the camera, a measurement is provided to the filter for that time step and can be used to update the estimated mean and covariance of the filter.

III. Methodology

A. Unscented Kalman Filtering

A combined UKF and Unscented Quaternion Estimator (USQUE) [34, 35], selected due to proven performance in previous work by the authors [32, 33], is implemented to estimate the attitude, angular velocity, and principal moments

of inertia of the debris. The debris attitude is determined through the USQUE portion of the filter, whereas the angular rates and principal moments of inertia are estimated through the standard UKF. After estimation, the estimated states are provided to the PID controller, which aims to maintain a safe post-capture system configuration, as will be detailed in Section III.B.

1. State Prediction

The states utilized by the UKF are 3 Euler error angles ($\boldsymbol{\delta p}$), 3 angular rates ($\boldsymbol{\omega}$), and 3 principal moments of inertia ($\boldsymbol{J}$). The three components of each of these vectors are such that the Euler error angles are $\boldsymbol{\delta p} = [\delta p_x, \delta p_y, \delta p_z]^T$, body-fixed angular rates are $\boldsymbol{\omega} = [\omega_x, \omega_y, \omega_z]^T$, and the principal moments of inertia are $\boldsymbol{J} = [J_x, J_y, J_z]^T$. The state vector is then given by $\boldsymbol{x} = [\boldsymbol{\delta p}^T, \boldsymbol{\omega}^T, \boldsymbol{J}^T]^T$.

The UKF creates a set of sigma points $\boldsymbol{\chi}_k$ at each time step k around the mean estimated states μ_k based on the covariance matrix P_k. The sigma points are calculated as:

$$\boldsymbol{\chi}_k(0) = \boldsymbol{\mu}_k = [\hat{\boldsymbol{\delta p}}_k^T, \hat{\boldsymbol{\omega}}_k^T, \hat{\boldsymbol{J}}_k^T]^T \tag{10a}$$

$$\boldsymbol{\chi}_k(i) = \boldsymbol{\sigma}_k(i) + \boldsymbol{\mu}_k \tag{10b}$$

where i denotes a particular sigma point and column of $\boldsymbol{\sigma}_k = \pm\sqrt{(n+\lambda)P_k}$. Variable n corresponds to the number of states of the filter and λ is given by $\lambda = \alpha^2(n+\kappa) - n$, where α and κ are tuning parameters. Parameter α controls the spread of the sigma point distribution and κ fine-tunes higher order moments. To obtain the matrix square root, the Cholesky decomposition of the covariance matrix P_k is utilized.

The sigma points are separated into 3 sections of 3 parameters according to $\boldsymbol{\chi}_k(i) = [\boldsymbol{\delta p}^T(i), \boldsymbol{\omega}^T(i), \boldsymbol{J}^T(i)]^T = [\boldsymbol{\chi}_k^{\delta p}(i), \boldsymbol{\chi}_k^{\omega}(i), \boldsymbol{\chi}_k^{J}(i)]$, representing the estimated states of the filter (as described earlier) at each sigma point. After providing an estimated quaternion attitude representation of the debris $\hat{\boldsymbol{q}}_0$, a spread of quaternion attitude representations $\boldsymbol{\chi}_k^q(i)$ is created according to the Euler error angles at each $\boldsymbol{\chi}_k^{\delta p}(i)$ point. The equations for this mapping $\boldsymbol{\chi}_k^{\delta p}(i) \rightarrow \boldsymbol{\chi}_k^q(i)$ can be found in prior work by Crassidis and Markley [34]. Once the conversion from Euler error angles to quaternions is completed, each sigma point (using the spread of quaternions instead of the Euler error angles) is propagated through the dynamics of the system according to Eq. (2), using the corresponding estimated states in place of the true states wherever applicable. As the moments of inertia of the debris are assumed constant, the dynamics for the moments of inertia are just set to 0.

After propagation, the $2n+1$ predicted sigma points $\boldsymbol{\chi}_{k+1}(i)$ are obtained by converting each of the predicted quaternions back to Euler angles. Again, the equations for $\boldsymbol{\chi}_{k+1}^q(i) \rightarrow \boldsymbol{\chi}_{k+1}^{\delta p}(i)$ can be found in prior work by Crassidis and Markley [34]. The mean predicted states and corresponding covariance matrix are calculated using the propagated $\boldsymbol{\chi}_{k+1}(i)$ points through:

$$\hat{\boldsymbol{x}}_{k+1}^- = \sum_{i=0}^{2n} W_i^{\text{mean}} \boldsymbol{\chi}_{k+1}(i) \tag{11a}$$

$$P_{k+1}^- = \sum_{i=0}^{2n} W_i^{\text{cov}} [\boldsymbol{\chi}_{k+1}(i) - \hat{\boldsymbol{x}}_{k+1}^-][\boldsymbol{\chi}_{k+1}(i) - \hat{\boldsymbol{x}}_{k+1}^-]^T + Q_{k+1} \tag{11b}$$

where Q is the process noise matrix and the weights W_i^{mean} and W_i^{cov} for the i-th sigma point are given by:

$$W_0^{\text{mean}} = \frac{\lambda}{n+\lambda} \tag{12a}$$

$$W_0^{\text{cov}} = \frac{\lambda}{n+\lambda} + (1 - \alpha^2 + \beta) \tag{12b}$$

$$W_i^{\text{mean}} = W_i^{\text{cov}} = \frac{1}{2(n+\lambda)}, \quad i = 1, 2, ..., 2n \tag{12c}$$

where β is the third tuning parameter that incorporates prior knowledge of the distribution.

2. Measurement Model and Filter Update

To update the predicted estimates $\hat{\boldsymbol{x}}_{k+1}^-$, the filter compares the mean predicted measurements $\hat{\boldsymbol{y}}_{k+1}$ to the received measurements $\tilde{\boldsymbol{y}}_{k+1}$ at each corresponding time step. The measurement model is given by:

$$\tilde{\boldsymbol{y}}_{k+1} = \boldsymbol{h}(\boldsymbol{x}_{k+1}) + \boldsymbol{v}_{k+1} \tag{13}$$

where $\boldsymbol{h}$ is the measurement model and $\boldsymbol{v}$ is the measurement noise vector consisting of Gaussian random variables with a mean of 0 and covariance R. The measurements, $\tilde{\boldsymbol{y}}$, are provided using a tension sensor model and a pinhole camera projection model where pixel coordinate measurements, $d_{x'}$ and $d_{y'}$, are generated for various tracked landmarks on the target at discrete observation times. The measurement model used by the system is given by:

$$\boldsymbol{h}(x_k) = \begin{bmatrix} T \\ d_{1,x'} \\ d_{1,y'} \\ d_{2,x'} \\ d_{2,y'} \\ \vdots \\ d_{w,x'} \\ d_{w,y'} \end{bmatrix} \tag{14}$$

where w denotes the total number of landmarks, and T is the magnitude of the tension in the tether. The tension model provides the magnitude of the tension as described in Eq. (5) - Eq. (7). The camera model for the landmarks is as described in Section II.C.

The predicted measurement corresponding to each sigma point in the UKF is generated using the measurement model according to $\boldsymbol{\gamma}_{k+1} = \boldsymbol{h}(\boldsymbol{\chi}_{k+1})$. The UKF predicts every possible measurement at each time step; however, the update step in the filter will only use the predicted measurements corresponding to the received measurements $\tilde{\boldsymbol{y}}_{k+1}$. This process is demonstrated in Fig. 3. The mean predicted measurement for all outputs, regardless of measurement availability, is given by $\hat{\boldsymbol{y}}_{e,k+1}$ and can be found through:

$$\hat{\boldsymbol{y}}_{e,k+1} = \sum_{i=0}^{2n} W_i^{\text{mean}} \boldsymbol{\gamma}_{k+1}(i) \tag{15a}$$

$$\boldsymbol{\gamma}_{k+1}(i) = \boldsymbol{h}(\boldsymbol{\chi}_{k+1}(i)) \tag{15b}$$

Once the sensor measurements at t_{k+1} are received by the UKF, the predicted measurement vector can be pruned for the available terms to obtain $\hat{\boldsymbol{y}}_{k+1}$ (see Fig. 3) by looping through all the possible measurement sources (i.e., each tracked landmark and the tension magnitude). Next, the output covariance, P_k^{yy}, and cross-correlation matrix, P_k^{xy}, are found by:

$$P_{k+1}^{yy} = \sum_{i=0}^{2n} W_i^{\text{cov}} \left[\boldsymbol{\gamma}_{k+1}(i) - \hat{\boldsymbol{y}}_{k+1}^-\right] \left[\boldsymbol{\gamma}_{k+1}(i) - \hat{\boldsymbol{y}}_{k+1}^-\right]^T \tag{16a}$$

$$P_{k+1}^{xy} = \sum_{i=0}^{2n} W_i^{\text{cov}} \left[\boldsymbol{\chi}_{k+1}(i) - \hat{\boldsymbol{x}}_{k+1}^-\right] \left[\boldsymbol{\gamma}_{k+1}(i) - \hat{\boldsymbol{y}}_{k+1}^-\right]^T \tag{16b}$$

During the calculation of P_k^{xy}, $\boldsymbol{\gamma}$ includes only the available measurement components rather than the entire predicted measurement vector. The innovation covariance, $P_{k+1}^{e_y e_y}$, and gain matrix, K_{k+1} are found using:

$$P_{k+1}^{e_y e_y} = P_{k+1}^{yy} + R_{k+1} \tag{17a}$$

$$K_{k+1} = P_{k+1}^{xy} (P_{k+1}^{e_y e_y})^{-1} \tag{17b}$$

The mean estimate and covariance are then updated using:

$$\hat{\boldsymbol{x}}_{k+1}^+ = \hat{\boldsymbol{x}}_{k+1}^- + K_{k+1}[\tilde{y}_{k+1} - \hat{y}_{k+1}^-] \tag{18a}$$

$$P_{k+1}^+ = P_{k+1}^- K_{k+1} P_{k+1}^{e_y e_y} K_{k+1}^T \tag{18b}$$

B. Controls

A relative distance PID control is employed to keep the tether taut such that there is always an applied moment on the target. The control action is designed to achieve a desired tether elongation δl with thrusters on the chaser

craft providing actuation with no error (i.e., perfect actuation). As the control requires the states of the target, it is implemented using a zero-order hold with the same period as the estimation (i.e., $\boldsymbol{U}$ is kept constant from step k to step $k+1$). The process variable at time step k for this controller is

$$e_k = \Delta l + l_0 - l_k^- \tag{19}$$

where l_k^- is the tether length calculated using the predicted quaternion at step k, $\hat{\boldsymbol{q}}_k^-$. The reason for using the predicted state is that it is assumed there is some delay between the time of measurement and its processing. The input magnitude is then calculated as

$$F_{u,k} = K_P e_k + K_I \int_0^{t_k} e_k dt + K_D \dot{e}_k \tag{20}$$

The proportional, derivative, and integral gains are given by the constants K_P, K_D, and K_I, respectively. Due to the discrete nature of the process variable, it is integrated using the trapezoidal rule from the initial to the current time step. The derivative of e_k is the negative of the tether length rate calculated using the predicted states, such that $\dot{e}_k = -\dot{l}_k^-$. With the consideration of saturation the control thrust is

$$\boldsymbol{U}_k = -\text{sat}(F_{u,k})\hat{\boldsymbol{V}}_{C,k} \tag{21}$$

with the saturation function

$$\text{sat}(F_{u,k}) = \begin{cases} U_{max} & \text{if} \quad F_{u,k} > U_{max} \\ F_{u,k} & \text{if} \quad U_{min} \leq F_{u,k} \leq U_{max} \\ U_{min} & \text{if} \quad F_{u,k} < U_{min} \end{cases} \tag{22}$$

where U_{max} and U_{min} are the upper and lower saturation limits respectively. The unit vector $\hat{\boldsymbol{V}}_{C,k}$ is the chaser velocity direction at time step k. This choice of thrust direction is consistent with lowering the orbit of the debris. With the consideration of saturation, the windup of the integrated error must be considered. Here, the integration of e_k is stopped if the control is saturated.

In addition to maintaining a relative distance, the chaser must also control its attitude in order to prevent the tether from winding about itself and to keep the target in frame. To this end, a sliding mode controller (SMC), akin to that in [36], is introduced to orient the chaser x-axis along the tether direction, $-\hat{\boldsymbol{e}}$. Thrusters on the chaser are assumed to apply only moments equal to the torque required by the SMC. The current implementation of this controller assumes perfect knowledge of the debris, such that the input torque is calculated during the integration of the system dynamics using the true states.

C. Online Estimation and Control Algorithm

The estimation and control are combined in MATLAB according to the algorithm presented in Fig. 3. After initializing the true system states $\boldsymbol{X}_0$ and estimated states $\hat{\boldsymbol{x}}_0^+$, the estimates are propagated from $\hat{\boldsymbol{x}}_k^+$ to $\hat{\boldsymbol{x}}_{k+1}^-$ where $k = 0, 1, ...N$. The control $\boldsymbol{U}_k$ is then calculated using the true systems states and the estimated states at t_k. The systems states are propagated through Eq. (3) from t_k to t_{k+1}, where, as previously stated, the control $\boldsymbol{U}_k$ is kept constant. The measurement update step then occurs, in which certain predicted measurements are discarded if they are unavailable. This needs to happen if a landmark is no longer in view of the camera, either from exiting the camera's field of view or by being occluded by other parts of the target, or if there is no measurement at t_{k+1}. The loop is then repeated until the estimates at t_N have been updated.

This algorithm permits the pixel coordinate and tension measurement frequencies to be different, which is to be investigated in the following Section. However, it does not take into account the duration of processing the estimates and measurements or the PID actuation capabilities itself, and as such is constrained to constant frequency measurements. While $\boldsymbol{U}_k$ could be calculated at a frequency different from that of the measurements, it was decided to calculate it at the fastest measurement frequency in this work.

IV. Simulation

The performance of the estimation and control will be evaluated by two Monte-Carlo simulations consisting of 1000 runs each, the true initial states of which are tabulated in Table 1 and the system parameters in Table 2. With these conditions and parameters, the initial tether elongation and alignment angle are -0.02 m and $\pi/6$ rad, respectively,

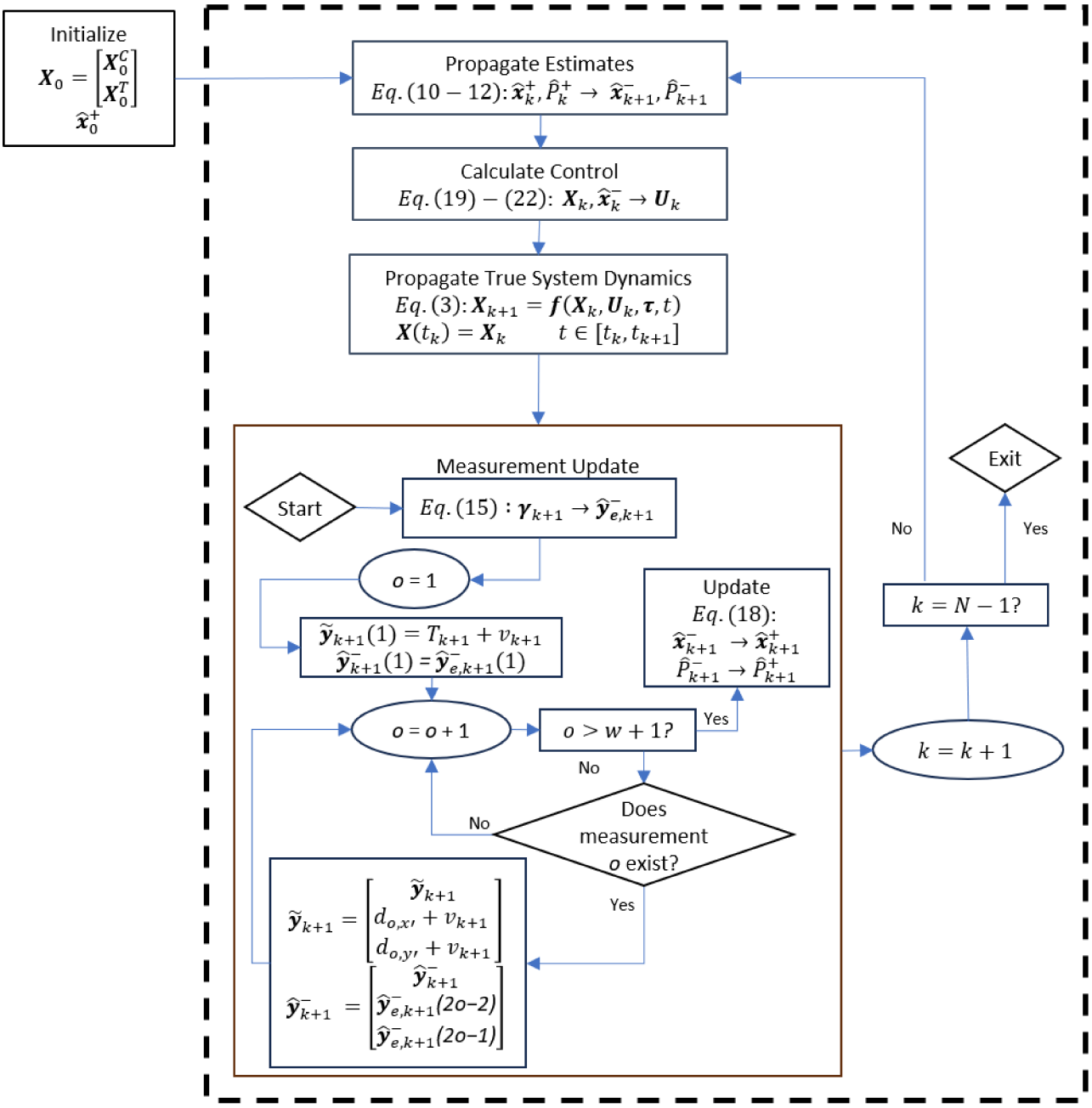

Fig. 3. Flowchart of the online estimation and control algorithm.

representing an imperfect capture. The individual Monte-Carlo runs are initialized with estimates calculated assuming a zero-mean Gaussian distribution with the standard deviations in Table 3 and an initial diagonal covariance matrix composed of the corresponding variances.

Table 1. Initial conditions for initially taut tether scenario.

Variable	Value
$\boldsymbol{R}_C$ (m)	$[-6176010.95, -420792.01, 2973766.68]^T$
$\boldsymbol{R}_T$ (m)	$[-6176021.75, -420810.02, 2973743.78]^T$
$\boldsymbol{V}_C$ (m/s)	$[-2457.79535, -4404.28547, -5712.40584]^T$
$\boldsymbol{V}_T$ (m/s)	$[-2457.76467, -4404.28338, -5712.420604]^T$
$\boldsymbol{q}_C$ (-)	$[-0.5564, 0.6637, 0.4699, 0.1708]^T$
$\boldsymbol{q}_T$ (-)	$[0.3213, -0.3830, -0.8138, 0.2962]^T$
$\boldsymbol{\omega}_C$ (rad/s)	$[0, 0, 0]^T$
$\boldsymbol{\omega}_T$ (rad/s)	$[0, 0.05, 0]^T$

Table 2. Chaser, Target, and Tether Parameters.

Parameter	Value
Chaser Inertia Matrix J_C (kg-m^2)	diag(83.3, 83.3, 83.3)
Target Inertia Matrix J_T (kg-m^2)	diag(15000, 3000, 15000)
Chaser Mass m_C (kg)	500
Target Mass m_T (kg)	3000
Tether Young's Modulus E (Pa)	60×10^9
Tether Diameter d (m)	0.001
Tether Natural Length l_0 (m)	30
Tether Damping c (Ns/m)	16
Tether Attachment Point, Chaser $\boldsymbol{r}_{tp,C}$ (m)	$[0.5, 0, 0]^T$
Tether Attachment Point, Target $\boldsymbol{r}_{tp,T}$ (m)	$[0, -0.875, 0]^T$

The standard deviations of the tension and pixel coordinate measurements are 10 N and 2 pixels, respectively. The tension values are selected based on the datasheet of existing tension sensors, whereas the pixel noise standard deviation is selected based on a value that seems reasonable from image processing methods. The pixel coordinates will be provided to the UKF by the camera model described in Section II.C with a focal length of 190 mm, sensor size of 20×11.25 mm, and a resolution of 1920×1080 pixels. The image space and world space scaling are therefore given by $s_{x'} = 1920/20$ pixels/mm and $s_{y'} = 1080/11.25$ pixels/mm. A total of 5 landmarks are chosen, consisting of the tether attachment point, two points on the side faces of the debris body, and two corners of the face on the negative $\hat{\boldsymbol{t}}_y$ direction, the coordinates of which are presented in Table 4 in the target body-fixed reference frame. The process noise matrix Q as well as the parameters α, β, and κ were tuned offline. The process noise matrix was tuned manually for the best estimation performance, resulting in $Q = \text{diag}(1 \times 10^{-32}$ (rad/s), 1×10^{-32} (rad/s), 1×10^{-32} (rad/s), 3×10^{-8} (rad/s^2), 3×10^{-8} (rad/s^2), 3×10^{-8} (rad/s^2), 0 (kg-m^2/s), 0 (kg-m^2/s), 0 (kg-m^2/s)). The other parameters were tuned using particle swarm optimization to minimize the final moment of inertia estimate errors across 10 Monte-Carlo simulations of a base scenario. The optimal values were found to be $\alpha = 0.22$, $\beta = 19.89$, and $\kappa = -6.03$. The chaser PID control is implemented with gains of $K_P = 300$ N/m, $K_I = 300$ N/ms, and $K_D = 2000$ Ns/m and saturation bounds of ±49.99 N. The two Monte-Carlo simulations in this paper differ in the measurement frequency of the camera, while the tension measurement frequency remains the same, at 10 Hz. The simulations will be denoted Case 1 and Case 2 in which the camera measurement frequency is 10 Hz and 1 Hz, respectively.

Table 3. Initial estimate standard deviations.

Estimate	Value
$\boldsymbol{\omega}$ (rad/s)	$[0.01, 0.01, 0.01]^T$
$\boldsymbol{\delta p}$ (rad)	$[0.01, 0.01, 0.01]^T$
$[J_x, J_y, J_z]^T$ (kg-m^2)	$[1250, 250, 1250]^T$

Table 4. Tracked feature position on target debris.

Feature	X Position (m)	Y Position (m)	Z Position (m)
Attachment Point, $r_{tp,T}$	0	-0.8750	0
Corner 1, C1	-0.6250	-0.8750	-0.6250
Corner 2, C2	0.6250	-0.8750	0.6250
Side 1, S1	-0.6250	-0.5833	0.4167
Side 2, S2	0.6250	-0.5833	0.4167

The true elongation and alignment angle at each timestep for all 1000 runs in Case 1 are reported in Fig. 4. The red lines indicate the minimum and maximum values of a quantity at a given time, while the black lines represent all other Monte-Carlo simulation values. It is clear that the estimation of the debris attitude and angular rates, which affect the calculation of l_k^- and $\dot{l}_k^-$, is precise as the elongation has a small distribution at a given time step. The elongation also approaches a steady-state value, further reducing this distribution. However, this transient elongation behavior is a result of the control being saturated as opposed to having better estimates as time passes. As can be seen in the zoomed portion of Fig. 4a, the elongation drops below zero after the tether becomes taut during some runs, which is unwanted for both the control and the estimation; however, this period of slackness is not significant enough to greatly impact the estimates. The alignment angle ψ displays behavior consistent with a constant thrust applied opposite to the chaser velocity direction. Such behavior is characterized by two frequencies: one higher – which is easily recognizable – and one lower, visible as the periodic rising and falling of the peak amplitude of the higher frequency (e.g., the increase in amplitude after approx. 350 s). It also stays well below the safety limit of 90° for all runs, indicating a degree of safety with the given control, which does not risk causing tether winding at the target's side.

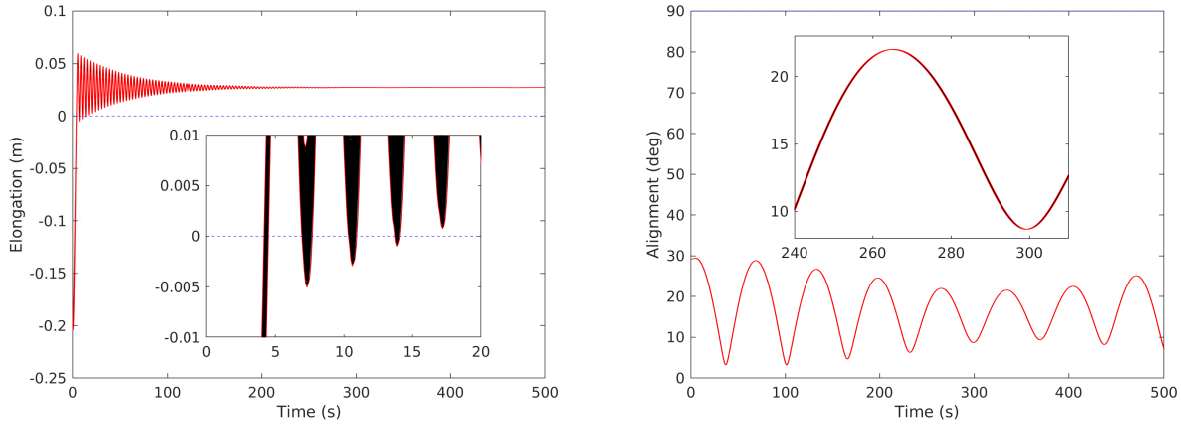

a Elongation **b Tether alignment angle**

Fig. 4. True elongation and alignment angles for every Monte-Carlo run in Case 1.

The Monte-Carlo distributions for the final moment of inertia estimates for Case 1 are presented in Fig. 5, along with

their respective means and standard deviations. The means are plotted as vertical black lines while the 3σ bounds are displayed as dashed black lines. The maximum 3σ deviations from the true moments of inertia are 4.7896%, 20.4137%, and 5.8626% for J_x, J_y, and J_z, respectively, indicating good convergence to the truth for J_x and J_z. The difference between the final mean and standard deviation percent errors of J_y and the other parameters is primarily a result of the difference in magnitude of the true moments of inertia. As the true J_y is 3000 kg-m^2 as compared to 15000 kg-m^2 for J_x and J_z, smaller errors will have larger percent differences. In addition, tension is unable to affect $\dot{\omega}_y$ of the target during the propagation of the sigma points due to the choice of tether attachment point. This makes J_y more difficult to observe, resulting in worse convergence.

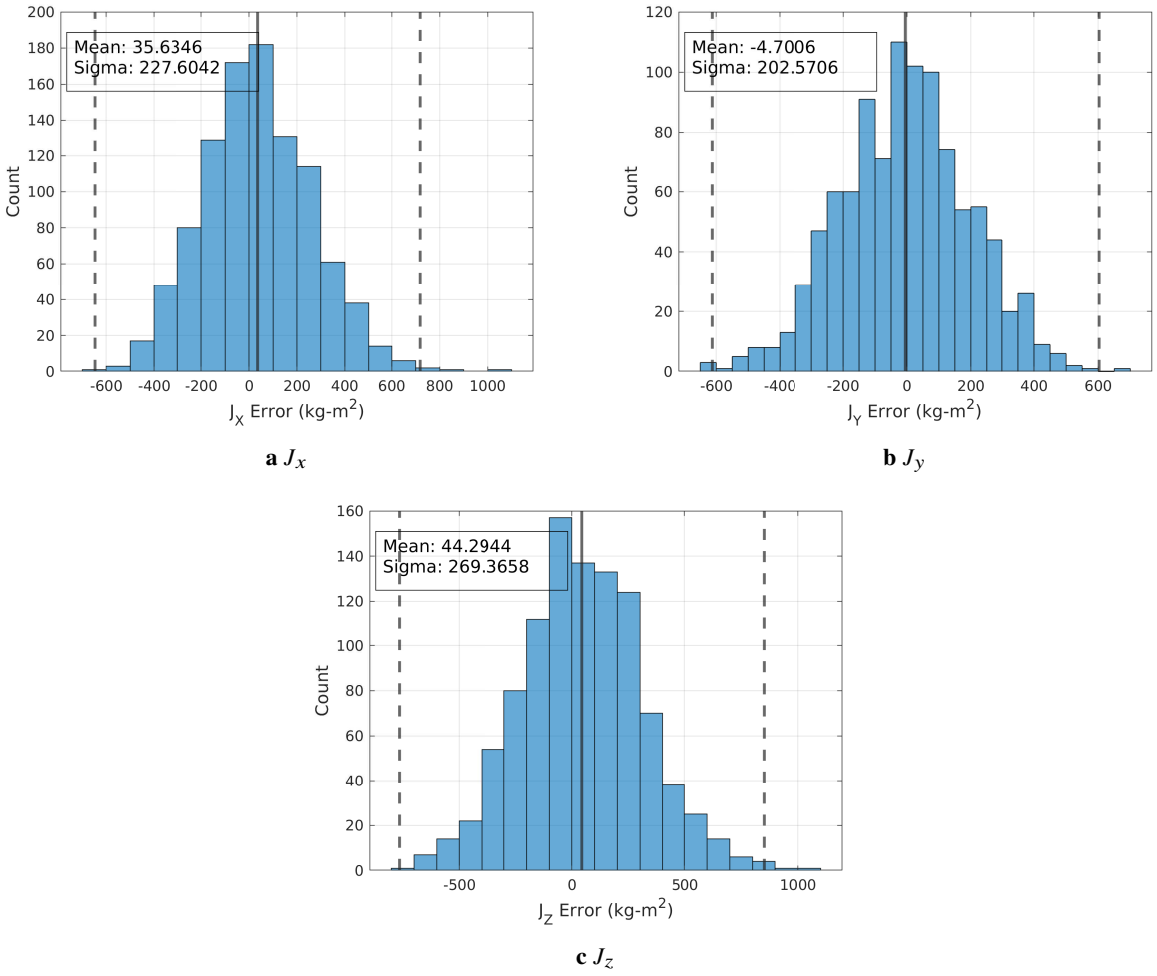

a J_x **b** J_y **c** J_z

Fig. 5. Final estimate Monte-Carlo distributions of the target moment of inertia parameters for Case 1.

Figure 6 displays the true elongation and alignment angles for Case 2. Similarly to Case 1, the elongation shows that the control is saturated for a significant portion of the simulation time. However, the less uniform distribution of the elongation as compared to Case 1, most clearly seen in the zoomed inset of Fig. 6a, indicates that the target attitude state estimation is worse in the first few seconds of the runs. This is primarily caused by the difference in pixel-coordinate measurement frequency of landmarks, which has been decreased by an order of magnitude from Case 1 to 2. While the noise associated with a given run will have an effect on this behavior, it is inconsequential compared to the impact of the pixel measurement frequency. The reduced accuracy of the state estimation during the first few seconds causes differences in the estimated length and length rate, affecting the control to become saturated earlier or later than those of Case 1. To illustrate the estimation accuracy difference, Fig. 7 displays the ω_z time histories of one run from both Case 1 and 2, along with the 3σ bounds for both the run and the entire Monte-Carlo simulation. It is clear that both the Monte-Carlo and predicted 3σ bounds for ω_z are greater in Case 2 during the first 50 s, which includes the period

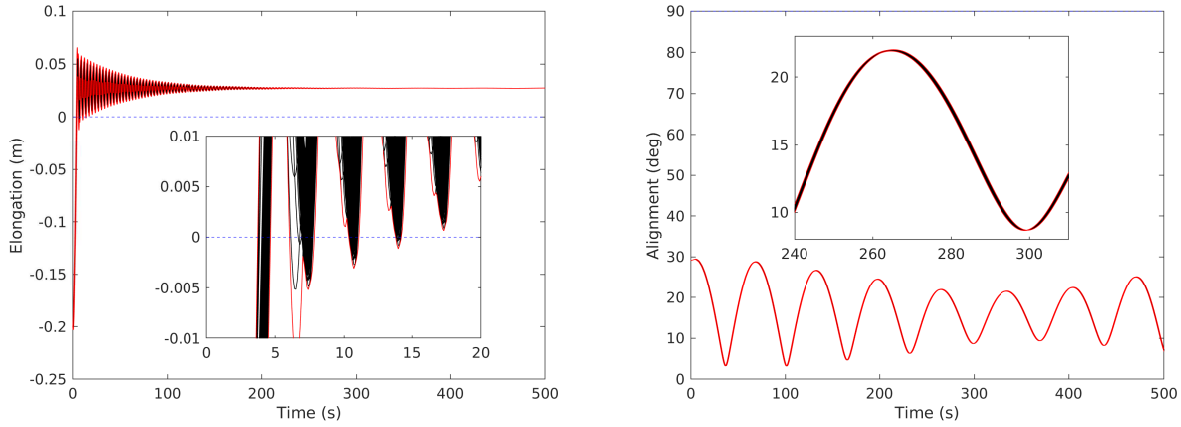

a Elongation **b Tether alignment angle**

Fig. 6. True elongation and alignment angle for every Monte-Carlo run in Case 2.

before control saturation. It should be noted, however, that after this initial 50 s transient period, the Monte-Carlo 3σ bounds remain similar in magnitude in the two cases.

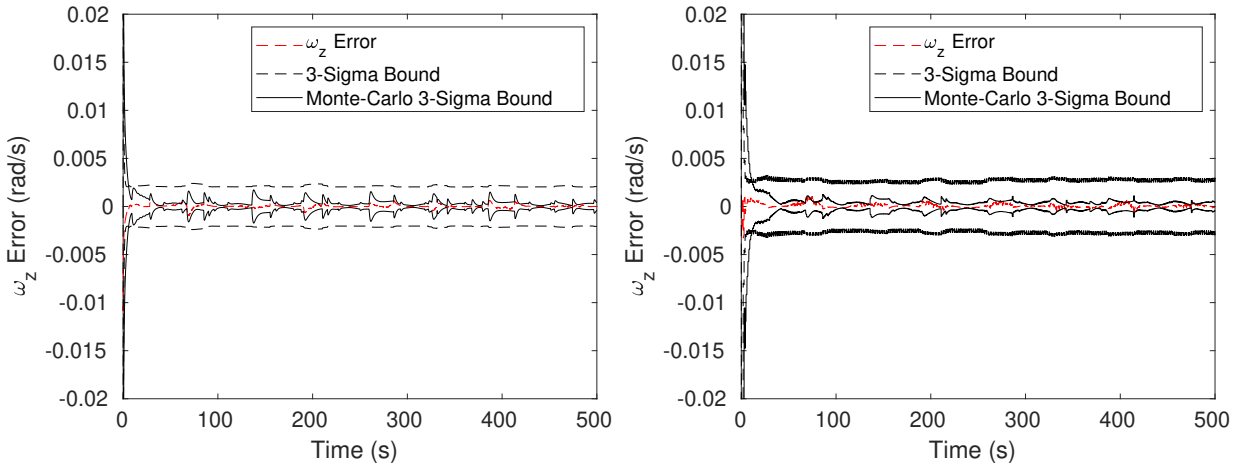

a Case 1 **b Case 2**

Fig. 7. Estimated ω_z time history for two individual Monte-Carlo runs from Cases 1 and 2.

The final moment of inertia estimate distribution for Case 2 is given in Fig. 8. It can be seen that the maximum 3σ deviations in the final inertia estimates are 5.4331%, 19.7899%, and 6.5875% for J_x, J_y, and J_z, respectively, which are not significantly different from Case 1. In contrast, the Monte-Carlo 3σ bounds are noticeably larger for the moments of inertia in Case 2, particularly in the first 50 s (see Fig. 9). However, after approx. 150 s the 3σ bounds in both cases have roughly the same behavior, indicating similar convergence properties given the PID control is saturated. The increased uncertainty during the first 50 s is expected due to the lower measurement update frequency from the camera in Case 2. Despite this lower update frequency and initial estimation performance, the filter is still capable of converging to approx. the same final estimates for the moments of inertia and is still able to obtain accurate attitude estimates of the debris (although slightly worsened as mentioned previously). Overall, although the update frequency causes some initial deviation in the elongation of the tether within the first 50 s, the final elongation in the tether remains approx. the same as in Case 1. In addition, the alignment angle of the debris also maintains a small deviation throughout the simulation (see Fig. 6b), which shows that safe orbital operations are still possible without perfect estimates.

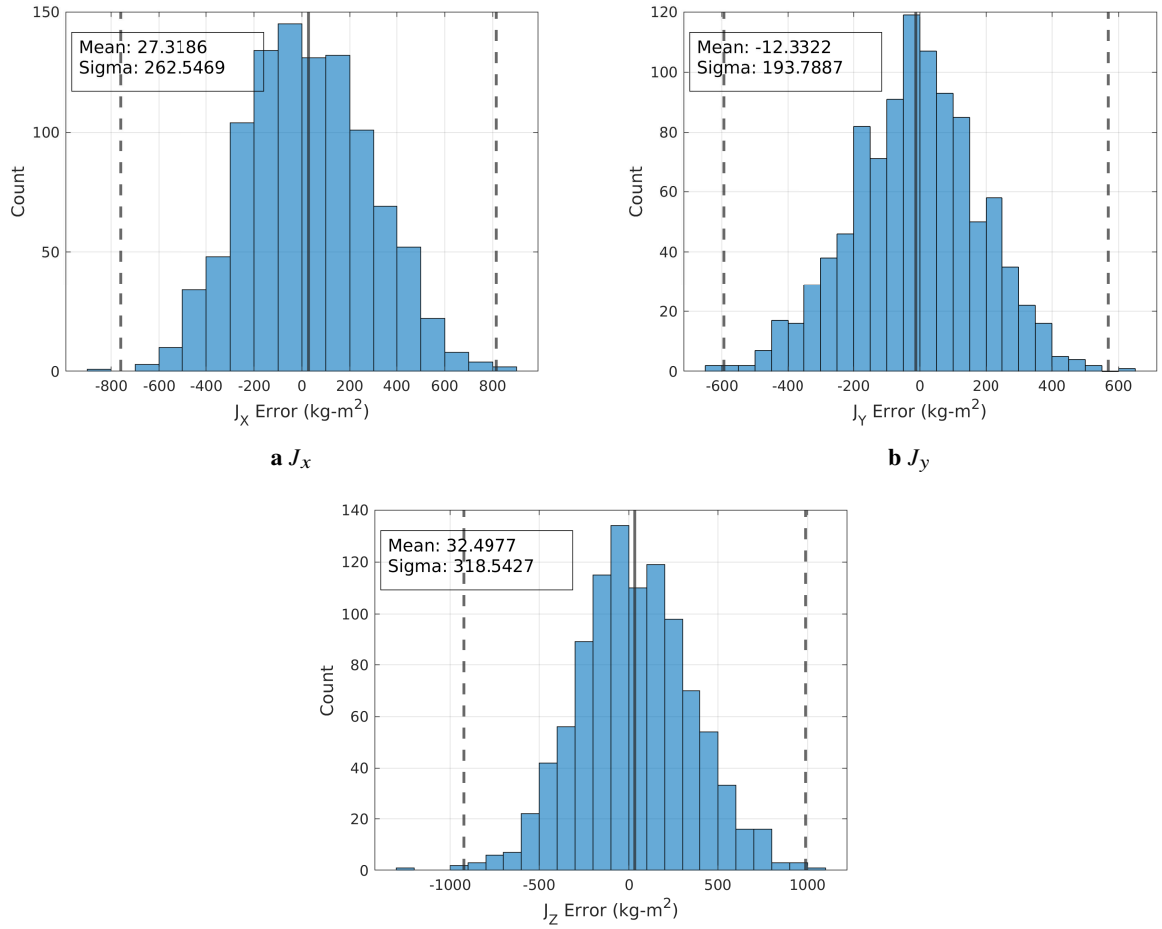

a J_x **b** J_y **c** J_z

Fig. 8. Final estimate Monte-Carlo distributions of the target moment of inertia parameters for Case 2.

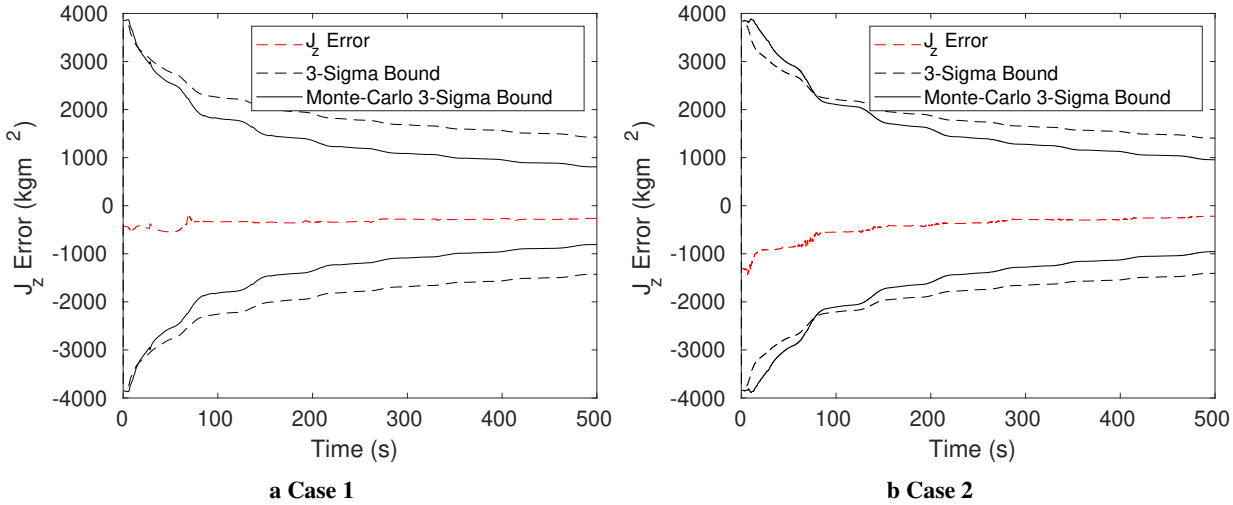

a Case 1 **b Case 2**

Fig. 9. Estimated J_z time history for two individual Monte-Carlo runs from Cases 1 and 2.

V. Conclusion

A previously developed UKF that estimates the attitude, angular rates, and principal moments of inertia of a debris object was implemented online during the simulation of a tethered ADR mission using measurements of tension and pixel coordinates of features on the target provided by a camera. The UKF is used in conjunction with a relative distance PID control to maintain safe operations post-capture. The performance of the estimation and control was evaluated through two Monte-Carlo simulations, which differed in the frequency of the camera measurements of the tracked feature points. In the first simulation, the measurement frequency was 10 Hz while it was 1 Hz in the second. The results indicate that the PID control could maintain safe conditions and provide sufficient tension when the control thrust was calculated using the predicted target state estimates, even with reduced camera measurement frequencies. The control profile permitted estimation to proceed, ultimately arriving at good estimates of the debris moment of inertia parameters after 500 s in both cases. The accuracy of the target y-axis principal moment of inertia estimate was on par with the other two in absolute terms, although it was significantly different in percent error. This could be remedied by changing the tether attachment point on the target, permitting greater observability of that principal moment of inertia.

The work in this paper represents another step towards a fully developed online estimation and control algorithm. The chaser's attitude control was calculated using the true target states, and as such the combined impact of the attitude and PID controllers on the safety of the mission and estimation capabilities could not be investigated. The future of this work lies in relaxing assumptions regarding the chaser's attitude control using the true states and the perfect knowledge of the target inertial position and velocity.

Acknowledgments

We would like to acknowledge Chris Gnam for his contribution to the camera and occlusion model used in this research. This work was funded by the National Science Foundation (NSF), under the CMMI Program, Award number 2105011. Derek and Liam both acknowledge the reception of the NASA Space Grant Fellowship.

References

[1] Liou, J.-C., and Johnson, N. L., "Instability of the present LEO satellite populations," *Advances in Space Research*, Vol. 41, No. 7, 2008, pp. 1046–1053. https://doi.org/10.1016/j.asr.2007.04.081.

[2] Miller, R., "Orbital Debris Quarterly News-Volume 25, Issue 4," *Orbital Debris Quarterly News*, Vol. 25, No. 4, 2021.

[3] Liou, J. C., Johnson, N. L., and Hill, N. M., "Controlling the growth of future LEO debris populations with active debris removal," *Acta Astronautica*, Vol. 66, No. 5-6, 2010, pp. 648–653. https://doi.org/10.1016/j.actaastro.2009.08.005.

[4] Bischof, B., "ROGER-Robotic geostationary orbit restorer," *54th International Astronautical Congress of the International Astronautical Federation, the International Academy of Astronautics, and the International Institute of Space Law*, Bremen, Germany, 2003. IAA–5.

[5] Wormnes, K., de Jong, J. H., Krag, H., and Visentin, G., "Throw-nets and tethers for robust space debris capture," *Proceedings of the 64th International Astronautical Congress*, Beijing, China, 2013. IAC-13, A6.5, 2x16445.

[6] Aslanov, V. S., and Yudintsev, V. V., "Behavior of tethered debris with flexible appendages," *Acta Astronautica*, Vol. 104, No. 1, 2014, pp. 91–98. https://doi.org/10.1016/j.actaastro.2014.07.028.

[7] Dudziak, R., Tuttle, S., and Barraclough, S., "Harpoon technology development for the active removal of space debris," *Advances in Space Research*, Vol. 56, No. 3, 2015, pp. 509–527. https://doi.org/10.1016/j.asr.2015.04.012.

[8] Lavagna, M., Pesce, V., and Bevilacqua, R., "Uncooperative objects pose, motion and inertia tensor estimation via stereovision," *Advanced Space Technologies for Robotics and Automation 2015*, Noordwijk, Netherlands, 2015.

[9] Aglietti, G. S., Taylor, B., Fellowes, S., Ainley, S., Tye, D., Cox, C., Zarkesh, A., Mafficini, A., Vinkoff, N., Bashford, K., Salmon, T., Retat, I., Burgess, C., Hall, A., Chabot, T., Kanani, K., Pisseloup, A., Bernal, C., Chaumette, F., Pollini, A., and Steyn, W. H., "RemoveDEBRIS: An in-orbit demonstration of technologies for the removal of space debris," *The Aeronautical Journal*, Vol. 124, No. 1271, 2019, pp. 1–23. https://doi.org/10.1017/aer.2019.136.

[10] Botta, E. M., Miles, C., and Sharf, I., "Simulation and tension control of a tether-actuated closing mechanism for net-based capture of space debris," *Acta Astronautica*, Vol. 174, 2020, pp. 347–358. https://doi.org/10.1016/j.actaastro.2020.04.052.

[11] Ru, M., Zhan, Y., Cheng, B., and Zhang, Y., "Capture Dynamics and Control of a Flexible Net for Space Debris Removal," *Aerospace*, Vol. 9, No. 6, 2022, p. 299. https://doi.org/10.3390/aerospace9060299.

[12] Aslanov, V. S., and Yudintsev, V. V., "Dynamics of large debris connected to space tug by a tether," *Journal of Guidance, Control, and Dynamics*, Vol. 36, No. 6, 2013, pp. 1654–1660. https://doi.org/10.2514/1.60976.

[13] Aslanov, V. S., "Chaos Behavior of Space Debris During Tethered Tow," *Journal of Guidance, Control, and Dynamics*, Vol. 39, No. 10, 2016, pp. 2399–2405. https://doi.org/10.2514/1.G001460.

[14] Aslanov, V. S., and Yudintsev, V. V., "Chaos in Tethered Tug–Debris System Induced by Attitude Oscillations of Debris," *Journal of Guidance, Control, and Dynamics*, Vol. 42, No. 7, 2019, pp. 1630–1637. https://doi.org/10.2514/1.G004162.

[15] Jasper, L., and Schaub, H., "Input shaped large thrust maneuver with a tethered debris object," *Acta Astronautica*, Vol. 96, 2014, pp. 128–137. https://doi.org/10.1016/j.actaastro.2013.11.005.

[16] Jaworski, P., Lappas, V., Tsourdos, A., Gray, I., and Schaub, H., "Debris Rotation Analysis During Tethered Towing for Active Debris Removal," *Journal of Guidance, Control, and Dynamics*, Vol. 40, No. 7, 2017, pp. 1769–1778. https://doi.org/10.2514/1.G002390.

[17] Peters, T. V., Briz Valero, J. F., Escorial Olmos, D., Lappas, V., Jakowski, P., Gray, I., Tsourdos, A., Schaub, H., and Biesbroek, R., "Attitude control analysis of tethered de-orbiting," *Acta Astronautica*, Vol. 146, 2018, pp. 316–331. https://doi.org/10.1016/j.actaastro.2018.03.016.

[18] Shan, M., and Shi, L., "Post-capture control of a tumbling space debris via tether tension," *Acta Astronautica*, Vol. 180, 2021, pp. 317–327. https://doi.org/10.1016/j.actaastro.2020.12.049.

[19] Qi, R., Misra, A. K., and Zuo, Z., "Active debris removal using double-tethered space-tug system," *Journal of Guidance, Control, and Dynamics*, Vol. 40, No. 3, 2017, pp. 722–730. https://doi.org/10.2514/1.G000699.

[20] Yudintsev, V., and Aslanov, V., "Detumbling space debris using modified yo-yo mechanism," *Journal of Guidance, Control, and Dynamics*, Vol. 40, No. 3, 2017, pp. 714–721. https://doi.org/10.2514/1.G000686.

[21] Wang, B., Meng, Z., and Huang, P., "Attitude control of towed space debris using only tether," *Acta Astronautica*, Vol. 138, 2017, pp. 152–167. https://doi.org/10.1016/j.actaastro.2017.05.012.

[22] O'Connor, W. J., and Hayden, D. J., "Detumbling of Space Debris by a Net and Elastic Tether," *Journal of Guidance, Control, and Dynamics*, Vol. 40, No. 7, 2017, pp. 1832–1836. https://doi.org/10.2514/1.G001838.

[23] Tweddle, B. E., "Computer vision-based localization and mapping of an unknown, uncooperative and spinning target for spacecraft proximity operations," Ph.D. thesis, Massachusetts Institute of Technology, 2013.

[24] Tweddle, B. E., Saenz-Otero, A., Leonard, J. J., and Miller, D. W., "Factor Graph Modeling of Rigid-body Dynamics for Localization, Mapping, and Parameter Estimation of a Spinning Object in Space," *Journal of Field Robotics*, Vol. 32, No. 6, 2015, pp. 897–933. https://doi.org/10.1002/rob.21548.

[25] Murotsu, Y., Senda, K., Ozaki, M., and Tsujio, S., "Parameter identification of unknown object handled by free-flying space robot," *Journal of Guidance, Control, and Dynamics*, Vol. 17, No. 3, 1994, pp. 488–494. https://doi.org/10.2514/3.21225.

[26] Ma, O., Dang, H., and Pham, K., "On-orbit identification of inertia properties of spacecraft using a robotic arm," *Journal of Guidance, Control, and Dynamics*, Vol. 31, No. 6, 2008, pp. 1761–1771. https://doi.org/10.2514/1.35188.

[27] Nguyen-Huynh, T. C., and Sharf, I., "Adaptive reactionless motion and parameter identification in postcapture of space debris," *Journal of Guidance, Control, and Dynamics*, Vol. 36, No. 2, 2013, pp. 404–414. https://doi.org/10.2514/1.57856.

[28] Zhang, T., Yue, X., Ning, X., and Yuan, J., "Stabilization and parameter identification of tumbling space debris with bounded torque in postcapture," *Acta Astronautica*, Vol. 123, 2016, pp. 301–309. https://doi.org/10.1016/j.actaastro.2016.04.007.

[29] Peng, J., Xu, W., Pan, E., Yan, L., Liang, B., and Wu, A.-g., "Dual-arm coordinated capturing of an unknown tumbling target based on efficient parameters estimation," *Acta Astronautica*, Vol. 162, 2019, pp. 589–607. https://doi.org/10.1016/j.actaastro.2019.03.008.

[30] Chu, Z., Ma, Y., Hou, Y., and Wang, F., "Inertial parameter identification using contact force information for an unknown object captured by a space manipulator," *Acta Astronautica*, Vol. 131, 2017, pp. 69–82. https://doi.org/https://doi.org/10.1016/j.actaastro.2016.11.019.

[31] Zhang, F., Sharf, I., Misra, A., and Huang, P., "On-line estimation of inertia parameters of space debris for its tether-assisted removal," *Acta Astronautica*, Vol. 107, 2015, pp. 150–162. https://doi.org/10.1016/j.actaastro.2014.11.016.

[32] Bourabah, D., Field, L., and Botta, E. M., "Estimation of uncooperative space debris inertial parameters after tether capture," *Acta Astronautica*, Vol. 202, 2023, pp. 909–926. https://doi.org/https://doi.org/10.1016/j.actaastro.2022.07.041.

[33] Bourabah, D., Gnam, C., and Botta, E. M., "Inertia tensor estimation of tethered debris through tether tracking," *Acta Astronautica*, Vol. 212, 2023, pp. 643–653. https://doi.org/10.1016/j.actaastro.2023.08.021.

[34] Crassidis, J. L., and Markley, F. L., "Unscented Filtering for Spacecraft Attitude Estimation," *Journal of Guidance, Control, and Dynamics*, Vol. 26, No. 4, 2003, pp. 536–542. https://doi.org/10.2514/2.5102.

[35] Crassidis, J. L., Markley, F. L., and Cheng, Y., "Survey of Nonlinear Attitude Estimation Methods," *Journal of Guidance, Control, and Dynamics*, Vol. 30, No. 1, 2007, pp. 12–28. doi:10.2514/1.22452.

[36] Crassidis, J. L., Vadali, S. R., and Markley, F. L., "Optimal Variable-Structure Control Tracking of Spacecraft Maneuvers," *Journal of Guidance, Control, and Dynamics*, Vol. 23, No. 3, 2000, pp. 564–566. https://doi.org/10.2514/2.4568.